RESEARCH ON COOLING HIGH-POWER MULTI-CORE PROCESSORS
Based on a Hybrid Micro-Channel Multiple Array Pin Fin Heat Sink

by

Zhengchu YANG[a], Shoujun SUN[b*], Dechang WANG[a], and Qinglu SONG[a,c]

[a]College of Mechanical and Electrical Engineering, Qingdao University, Qingdao, China
[b]National Engineering Research Center of Digital Home Networking, Qingdao, China
[c]School of Energy and Environment, City University of Hong Kong, Hong Kong, China

Original scientific paper
https://doi.org/10.2298/TSCI251128026Y

With the increasing power density of modern processors, effective management of hotspot temperatures has become a critical challenge in thermal design. This study proposes a novel hybrid micro-channel heat sink incorporating multiple arrays of cylindrical pin fins for efficient thermal regulation in multi-core processors operating under high heat flux. The proposed design utilizes rectangular micro-channels in regions of low heat flux (common zones) and integrates cylindrical pin fin arrays in high heat flux regions (hotspots) to enhance localized cooling performance. The thermal performance of this hybrid structure is evaluated numerically based on key metrics, including thermal resistance, R_{tot}, pressure drop, $\Delta p_{max,ch}$ and $\Delta p_{avg,ch}$, pumping power, P_{tot}, temperature non-uniformity, δT_{hs} and δT_{bot}, maximum temperature at hotspot, $T_{max,hs}$, and entropy production, S. Additionally, to examine the influence of thermophysical properties of refrigerants on heat sink performance, the study simulates and compares the phase change cooling characteristics of several commonly used organic refrigerants. Compared to the hybrid micro-channel heat sink with a single pin fin array, the multiple array structure achieves similar pressure drop and pumping power, while reducing thermal resistance and S by 4% and 7%, respectively. In contrast, δT_{hs} and δT_{bot} are reduced by approximately 30%-50%.

Keywords: *cooling, micro-channel, multiple array pin fin, hybrid heat sink*

Introduction

Intel invented the world's first processor in 1971, which was made up of 2300 transistors, and so far, processors containing more than 5.4 billion transistors have been developed [1]. The increase in design complexity and dynamic power consumption of single-core processors promotes the development of processor design architecture towards multi-core technology. At these cores, the heat flux far exceeds the surrounding area, forming a high hotspot area that greatly affects the normal operation and service life of the processor. Fazeli and Vafai [2] pointed out that when the processor temperature reaches 80 °C or more, the operational reliability of the processor decreases by 5% as the temperature increases by 1 °C. Hu *et al*. [3] also

*Corresponding authors, e-mail: sql@qdu.edu.cn; sunshoujun@haier.com

pointed out that after a certain temperature is reached, processor efficiency has a negative correlation with temperature. Therefore, it is very important to study and develop the heat dissipation of high heat flux components.

Traditionally, a significant number of processors have relied on air cooling systems. However, as processor power consumption continues to rise, air-based thermal management is increasingly insufficient to meet modern heat dissipation demands. Based on Zhou *et al*. [4], air cooling progressively fails to satisfy the thermal requirements of high performance processors. Since the concept of micro-channel was first proposed, its heat transfer area to volume ratio and significant inlet effect provide superior heat dissipation performance. Since then, micro-channel technologies have gained traction in processor cooling applications. Cao and Wu [5] provided a comprehensive overview of the development and classification of micro-channel heat sinks. Dong *et al*. [6] compared single-layer and double-layer micro-channels, demonstrating the enhancement of heat transfer by double-layer micro-channels. Shang *et al*. [7] pointed out the surface enhancement technology and mechanism of micro-channels, and proved that changing the structure of the micro-channel itself is an important way to improve the performance. Zhao *et al*. [8] studied and summarized the application of high thermal conductivity polymer materials in heat sinks. Yang *et al*. [9] and Kim *et al*. [10] explored single-phase cooling mechanisms using micro-channels. Su [11] and Alireza [12] investigated multi-phase cooling, demonstrating through experiments that phase change cooling significantly outperforms single-phase methods in thermal efficiency. Xu *et al*. [13] conducted a comparative experimental analysis on refrigerants R134a, R1234yf, and R1234ze(E), examining heat transfer coefficients under varied flow rates, heat flux densities, and saturation pressures, with a focus on flow boiling characteristics. Rostami *et al*. [14] examined PCM, while Deng *et al*. [15] proposed a novel graphene nanosheet-based flexible composite PCM for chip-level thermal management. Jet cooling, as an advanced enhancement technique to micro-channel cooling, was explored by Patel *et al*. [16] and Deng *et al*. [17], with the aim of achieving superior heat dissipation at higher flow rates.

In recent years, pin fin structures have garnered considerable attention due to their capacity to enhance heat transfer by increasing the fluid-solid interaction surface area and promoting flow disturbance [18, 19]. However, there are still some limitations in the existing research when facing the practical application of non-uniform thermal field on multi-core processors. For example, Ansari and Kim [20] proposed a hybrid micro-channel pin fin (H-MPF) heat sink to significantly improve the local heat transfer, but its single array design is not suitable for multi-core processors. Vilarrubi *et al*. [21] used a variable-density pin fin structure to improve the surface temperature uniformity, but the complex density gradient may increase the difficulty of manufacturing, and the differentiated arrangement was not clearly based on the core layout. Feng *et al*. [22] proposed annular-cavity micro-pin fins, which reduce the flow dead zone, but its topology still focuses on global strengthening and does not reflect the targeted research on multiple hotspots. Wang *et al*. [23] introduced a multi-layer tree-like micro-channel heat sink structure that eliminates non-branching regions common in traditional micro-channel designs, but its complex 3-D flow channel faces challenges in process integration and pressure drop control. In addition to the arrangement and number of pin fins, the shape of the cross-section is also a key factor affecting the heat dissipation performance. For example, through CFD simulations, Danismaz [24] found that the elliptical pin fin can improve the hydro-thermal performance factor by 90% compared with the traditional round pin fin, mainly due to its larger first contact area and enhanced flow disturbance.

This study presents a novel hotspot-targeted cooling architecture that integrates micro-channels with multiple arrays of pin fins to enable effective thermal management in multi-core processors. The proposed structure avoids the fabrication complexity that may be introduced by the design while achieving finer local thermal control than a single array design, which is beneficial to alleviate thermal stress at the edge of the array and cope with different processor core layouts.

This study is the first to systematically analyze the entropy generation of this hybrid multi-array structure, and it is clear that its performance advantage mainly stems from the reduction of heat transfer irreversible entropy generation. At the same time, from the verification of single-phase water cooling performance to the potential evaluation of phase change refrigerants, using the verified structure, it is proven that the refrigerants with low vapor density and high latent heat have better phase change cooling performance, which provides an important reference for engineering applications under extreme heat flux. Together, these works promote the development of energy-efficient and engineerable heat dissipation design for non-uniform heat flux.

Heat sink models

Micro-channel heat sink

Figure 1 illustrates the design of a non-hybrid rectangular micro-channel (NH-RM) heat sink consisting of 18 micro-channels. In a NH-RM heat sink design, the entire heat sink only consists of rectangular micro-channels to cool the hotspot and the common areas at the bottom, as shown in fig. 1(a), the hotspot (shown in orange in the center of the bottom surface of the heat sink) and other areas on the underside of the heat sink except the hotspot area as shown in fig. 1(b), and the geometric parameters of the micro-channel as shown in fig. 1(c).

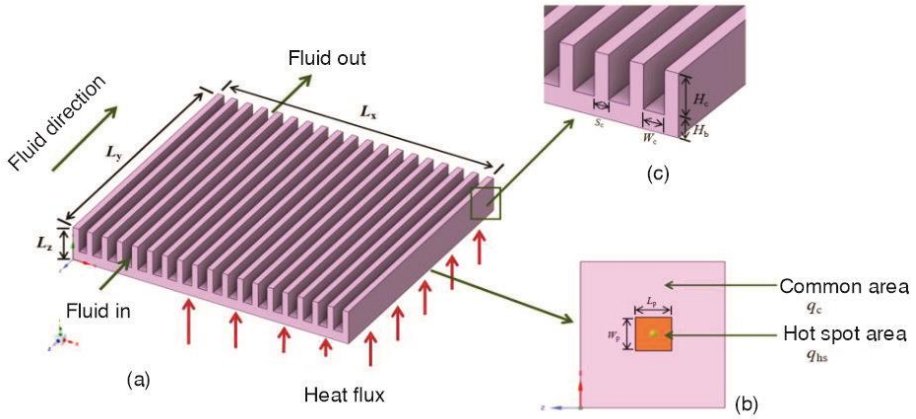

Figure 1. Diagrams of (a) NH-RM heat sink, (b) heat sink bottom view, and (c) geometric parameters of the micro-channels

The values of all geometric parameters of the micro-channel heat sink are shown in tab. 1, the unit in the table is mm. In this study, the non-hybrid micro-channel heat sink and the H-MPF heat sink have the same heat sink size.

In the numerical simulation, water was used as the coolant, which has the characteristics of low saturation temperature and green environmental protection. Silicon was selected

as the micro-channel material, and the thermal physical properties of the material and coolant are shown in tab. 2.

Table 1. Dimensions of micro-channel and hotspot

Micro-channel dimensions [mm]								
L_x	L_y	L_z	H_c	H_b	S_c	W_c	L_p	W_p
10	10	1	0.7	0.3	0.2	0.3	2	2

Table 2. The thermal physical properties of the material and the coolant

Part	Material	ρ [kgm^{-3}]	C_p [Jkg^{-1}K^{-1}]	k [Wm^{-1}K^{-1}]	μ [Pa s]
Heat sink	Silicon	2330	712	148	–
Coolant	Water	997	4180	0.607	8.9×10^{-4}

Hybrid micro-channel pin fin heat sink

Figure 2 illustrates the design of a H-MPF heat sink consisting of 18 micro-channels and pin fin matrices, the arrangement of the pin fin is 10×10, and the position of the pin fin is precisely consistent with the position of the hotspot on the bottom of the heat sink.

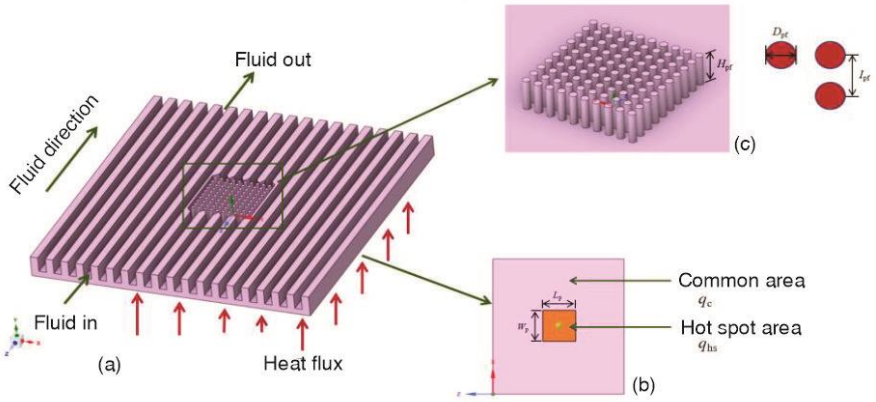

Figure 2. Diagram of a H-MPF heat sink

As shown in figs. 1(b) and 2(b), the heat flux in the hotspot area at the bottom of the heat sink is 300 W/cm^2, that in the common area is 50 W/cm^2, the velocity of the inlet fluid varies from 0.3 m/s (Re = 100) to 3 m/s (Re = 1000), and the heat dissipation performance of the hybrid heat sink is numerically simulated in this range.

Previous studies [25, 26] have shown that the arrangement method, spacing, and number of pin fins have obvious effects on the heat dissipation performance of the heat sink. As shown in fig. 3(a), we split the pin fin array into multiple identical new pin fin arrays. Similarly, as shown in fig. 3(b), we visually split the processor into multiple identical small processors. In this study, they are referred to as H-MPF (single array) and H-MPF (multiple array) heat sinks, respectively. Four 5×5 pin fin arrays were designed for the study, and there was a strict one-to-one correspondence between the location and size of hotspots and the pin fin array, with each pin fin having a diameter of 0.1 mm and a spacing of 0.2 mm. The size of each hotspot was 1 mm×1 mm.

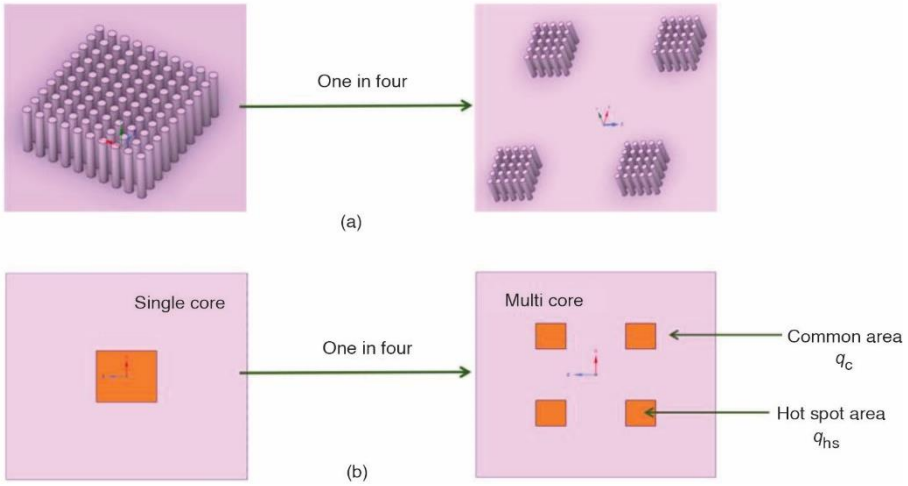

Figure 3. Diagrams of different arrangements of pin fin array

Numerical analysis

Numerical scheme

In this study, ANSYS Fluent 2023 R1 software is used to simulate the heat transfer of heat sinks. This method can effectively reduce the time for the simulation to reach convergence while solving the fluid equation. The convergence residual standard of continuity equation, energy simulation, and momentum equation in the simulation is set to 10^{-6}. To simplify the simulation calculation and minimize the running time of the simulation, the following assumptions were made in this study:

- *The simulation state was steady*. This study aims to evaluate the final performance of the heat sink under a high heat flux rather than a transient start-up process, and this assumption significantly reduces the computational complexity.
- *The flow state of the fluid is laminar flow*. The Reynolds number range for all simulations was set to 100 to 1000, which is completely in the laminar interval of the flow within the micro-channel. In this Reynolds number range, the results of the laminar and turbulent models are generally consistent.
- *Fluid is incompressible*. For a single-phase flow with water as cooling and limited temperature rise range, the density change is extremely small, and the change of physical properties such as specific heat capacity and thermal conductivity with temperature is usually negligible).
- Ignoring radiation heat transfer.
- The solid material is a constant thermophysical parameter.
- The heat flux of the hotspot is constant.
- Constant inlet fluid temperature. The initial $T_{f,in}$ is set to 300 K.

There are key research objects in this study: total thermal resistance R_{tot} (measures the overall heat conductivity of the heat sink from the heat source to the cooling fluid, with lower values indicating higher heat dissipation efficiency), average pressure drop Δp_{avg} (index of the mechanical energy consumed by the fluid to overcome the flow resistance), total pumping power P_{tot} (the external input work required to maintain the flow, together with Δp_{avg}, defines the *fluid delivery cos*t of the cooling system) and temperature non-uniformity δT (δT_{hs}: mean absolute temperature deviation (MATD) calculated only for the local hotspot region, which

quantifies the temperature distribution inside the hotspot, δT_{bot}: MATD calculated for the entire heat sink bottom surface, including hotspots and common areas). The expression for R_{tot} is as:

$$R_{tot} = \frac{T_{max,s} - T_{f,in}}{Q_{tot}} \tag{1}$$

where $T_{max,s}$ and $T_{f,in}$ are the maximum temperatures at the base of the heat sink (solid) and fluid temperature at the inlet (300 K), respectively, Q_{tot} – the total heat applied at the base of the heat sink (solid), which is expressed as:

$$Q_{tot} = q_c A_c + q_{hs} A_{hs} \tag{2}$$

where q_c and q_{hs} are the heat flux densities of the common area and the hotspot area on the underside of the heat sink, respectively. The area corresponds to A_c and A_{hs}, respectively.

In this paper, the MATD is introduced to evaluate the non-uniformity of temperature. MATD can be used to calculate the non-uniformity of temperature in a certain region. The temperature non-uniformity at the hotspot is expressed as [27]:

$$\delta T_{hs} = \frac{|T_{max,hs} - T_{avg,hs}| + |T_{min,hs} - T_{avg,hs}|}{2} \tag{3}$$

where $T_{max,hs}$, $T_{avg,hs}$, and $T_{min,hs}$ are the maximum, average, and minimum temperatures at the hotspot. The smaller δT_{hs} is, the better the temperature uniformity of the hotspot.

The expression for Δp_{avg} is as:

$$\Delta p_{avg} = p_{inlet} - p_{ouelet} \tag{4}$$

The total pumping power P_{tot} is as:

$$P_{tot} = n_{ch} u_{avg} A_c \Delta p_{avg,ch} \tag{5}$$

where n_{ch} is the total number of channels, u_{avg} – the average inlet velocity of fluid, A_c – the cross-sectional area of a channel, and $\Delta p_{avg,ch}$ – the average pressure drop across a single channel.

Boundary conditions

Figure 4 shows the boundary conditions of the model, which include the inlet and outlet, the solid-liquid interface, the heat source, and the external wall.

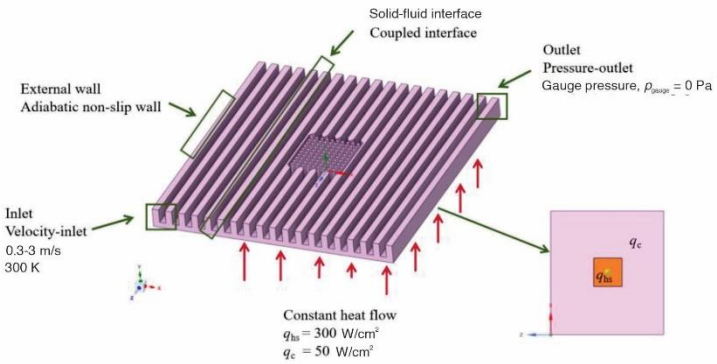

Figure 4. Model boundary conditions

Governing equations

Continuity equation:

$$\nabla(\rho_{\mathrm{f}}\bar{V}) = 0 \tag{6}$$

Momentum equations:

$$\bar{V}\nabla\left(\rho_{\mathrm{f}}\bar{V}\right) = -\nabla p + \nabla\left(\mu_{\mathrm{f}}\nabla\bar{V}\right) \tag{7}$$

Energy equation:

$$\bar{V}\nabla\left(\rho_{\mathrm{f}}C_p T_{\mathrm{f}}\right) = \nabla\left(k_{\mathrm{f}}\nabla T_{\mathrm{f}}\right) \tag{8}$$

The energy equation in the solid domain is expressed as:

$$\nabla\left(k_{\mathrm{s}}\nabla T_{\mathrm{s}}\right) = 0 \tag{9}$$

The temperature continuity equation for the coupling of the liquid-solid interface is expressed as:

$$k_{\mathrm{l}}\frac{\partial T_{\mathrm{l}}}{\partial n} = k_{\mathrm{s}}\frac{\partial T_{\mathrm{s}}}{\partial n} \tag{10}$$

Grid independence verification

Figure 5 illustrates that both the solid and fluid domains are discretized using a fine, unstructured polyhedral grid. Within the fluid domain, multi-layers of refined mesh elements are generated in proximity to the walls to resolve boundary layer flow characteristics. To ensure grid-independent simulation results, a grid independence study is conducted for both the micro-channel heat sink and the H-MPF heat sink.

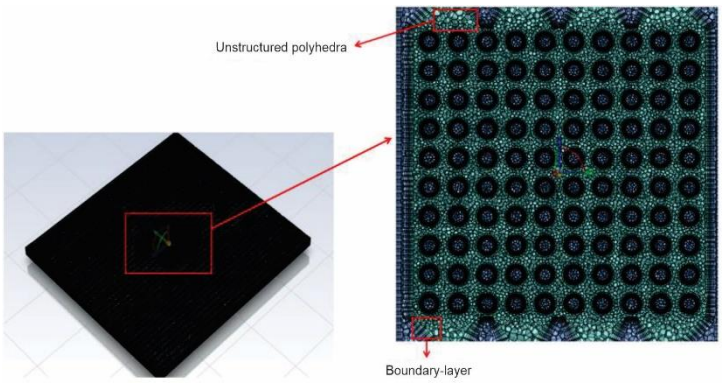

Figure 5. The H-MPF heat sink structured grid

Since the H-MPF (single array) and H-MPF (multiple array) hybrid heat sinks have identical physical structures, only one of them is selected for verification in the grid independence verification. The H-MPF (single array) heat sink is analyzed at different mesh densities, ranging from 1 to 9 million nodes, as shown in fig. 6(a), as the number of grids increased from 6.4 to 9 million, the maximum temperature at the hotspot only increased by 0.02 K, the maximum pressure drop increased by 0.037 kPa, so to balance simulation accuracy and computational efficiency, chose about 6.4 million grid cells as the optimal solution. NH-RM heat sink

is analyzed at different mesh densities, ranging from 0.8 to 7.7 million nodes, as shown in fig. 6(b), as the number of grids increased from 4.1 to 7.7 million, the maximum temperature at the hotspot only increased by 0.018 K, the maximum pressure drop increased by 0.021 kPa, so to balance simulation accuracy and computational efficiency, we chose about 4.1 million grid cells as the optimal solution.

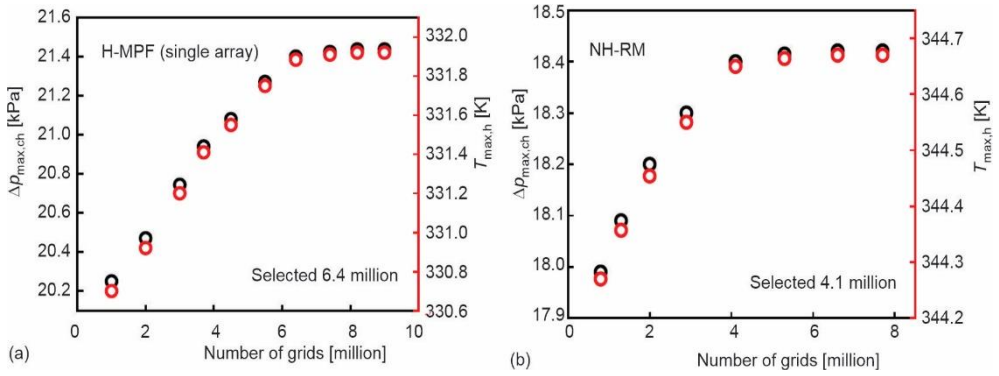

Figure 6. Grid independence verification;
(a) H-MPF verification and (b) NH-RM verification

Numerical model validation

To further validate the reliability of the numerical model, a laminar flow model verification is conducted in this section, and the simulation results are compared with experimental data from previous studies. Figure 7 presents the pressure drop and maximum temperature of the hotspot between laminar flow models and conventional turbulence models across a range of Reynolds number (from 100-1000). The results show that the calculation results of several turbulence models are consistent with those of laminar flow models. Therefore, it can be inferred that the flow rate in the H-MPF and NH-RM heat sink (Re = 100-1000) will not exceed the critical value of turbulence. As shown in figs. 7(a) and 7(c), as Reynolds number changes from 100-1000, the average pressure drop of the H-MPF (multiple array) heat sink and the NH-RM heat sink increases from 1.9-21.3 kPa and 0.8-19 kPa, respectively. As shown in figs. 7(b) and 7(d), as Reynolds number changes from 100-1000, the maximum temperature of the hotspot of the H-MPF (single array) heat sink and the NH-RM heat sink decreases from 334-324 K and 353-339 K, respectively.

Figure 8(a) shows a good overall agreement between the numerical results of this study and numerical results of Fu *et al*. [28] and experimental results of Ansari and Kim [20] concerning the non-uniformity of the hotspot temperature of the H-MPF heat sink; and their maximum errors are 4.7% for Re = 1000 and 5% for Re = 400, respectively. Figure 8(b) compares the numerical results of this study and numerical results of Fu *et al*. [28] and experimental results of Qu [29] concerning the average pressure drop of the micro-channel heat sink and their maximum errors are 8% for Re = 800 and 7% for Re = 770, respectively. These experimental and numerical results investigate the behavior of fluid-flow in a micro-channel heat sink and a hybrid micro-channel fin pin heat sink over a wide range of Reynolds number, including the pressure drop of the fluid and the resulting non-uniformity of temperature. The results show that the numerical calculation results of this paper are in good agreement with the data in the existing literature, verifying the accuracy of the model in this study.

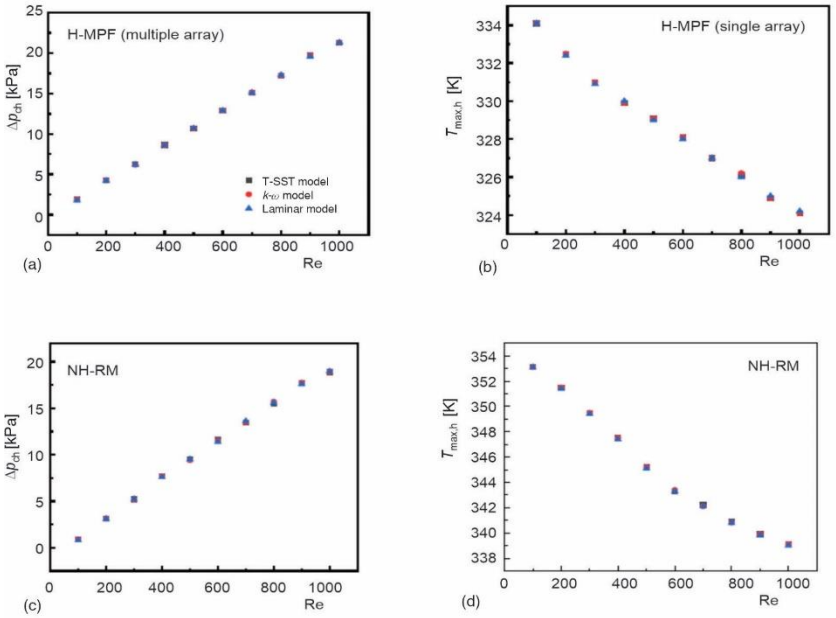

Figure 7. Verification of flow state under different Reynolds number; (a) average pressure drop of the H-MPF, (b) hotspot maximum temperature of the H-MPF, (c) average pressure drop of the NH-RM, and (d) hotspot maximum temperature of the NH-RM

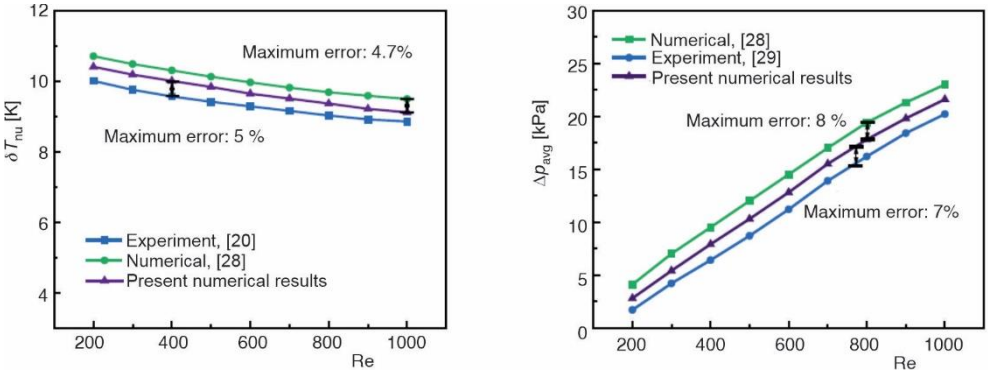

Figure 8. Validations of numerical results; (a) results of [20, 28] for the non-uniformity of temperature with Reynolds number ranging from 200-1000 and (b) results of [28, 29] for the drop in pressure with Reynolds number ranging from 200-1000

Results and discussion

Heat sink performance analysis

Temperature field analysis

Several studies have investigated the mechanism of heat transfer in hybrid heat sinks with different micro-channel arrangements (linear and staggered) and pin fin shapes (cylindrical,

hexagonal, trapezoidal, *etc.*) [30, 31]. In this study, the primary focus is on evaluating the heat dissipation performance of the proposed hybrid micro-channel single/multiple array pin fins heat sink. Furthermore, the maximum heat flux that can be sustained in the hotspot region by the NH-RM, H-MPF (single array), and H-MPF (multiple array) heat sinks is compared. Given that the H-MPF (multiple array) heat sink features a completely symmetric geometry, only half of the structure is selected for numerical analysis to reduce computational complexity.

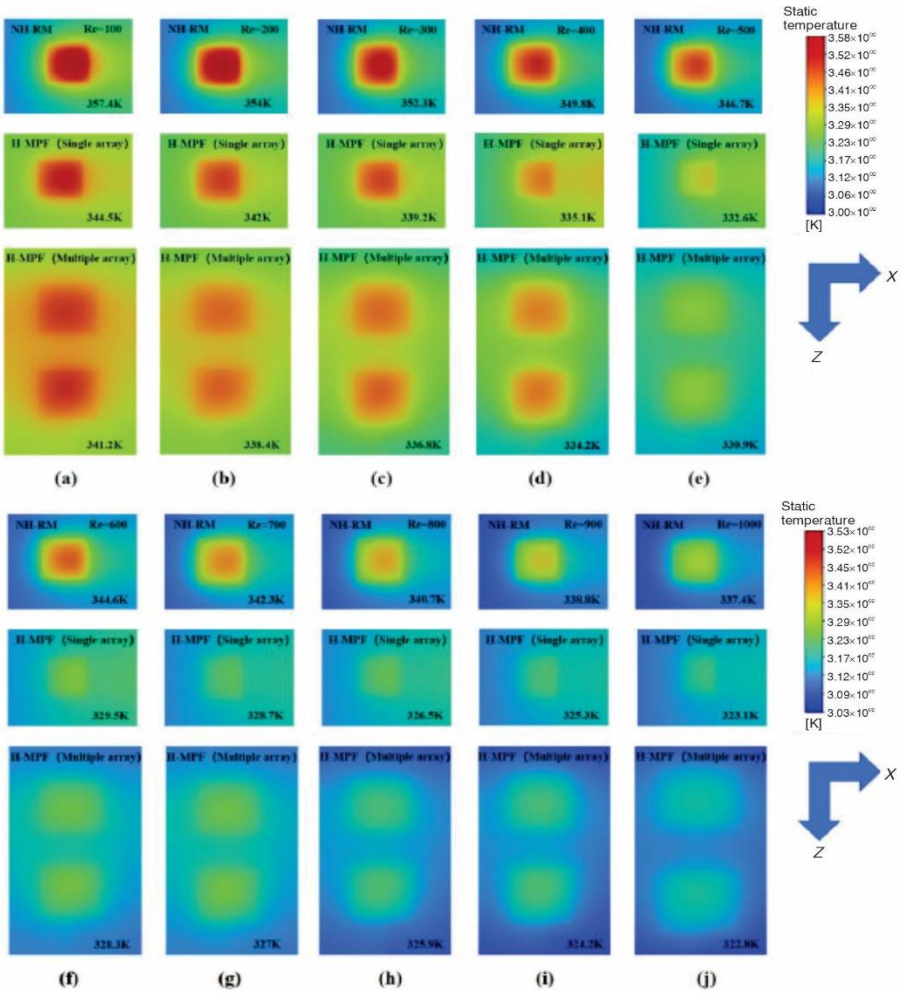

Figure 9. Temperature profiles at the bottom of the heat sink (*z-x* plane, $L_y/y = 0$) for NH-RM, H-MPF (single array), and H-MPF (multiple array) at different Reynolds number; (a) Re = 100, (b) Re = 200, (c) Re = 300, (d) Re = 400, (e) Re = 500, (f) Re = 600, (g) Re = 700, (h) Re = 800, (i) Re = 900, (j) Re = 1000

Figure 9 illustrates the local temperature distributions at the base of the heat sink (*z-x* plane, $L_y/y = 0$), covering both hotspot and common areas, for three structures: NH-RM, H-MPF (single array), and H-MPF (multiple array). The range of Reynolds number is from 100-1000. The results indicate a notable enhancement in temperature uniformity on the bottom surface following the incorporation of pin fins, particularly in the hybrid designs. The formation

of localized heat accumulation prominent in the NH-RM structure is effectively mitigated, as the maximum hotspot temperature, $T_{max,hs}$, is significantly reduced with the hybrid structures.

In fig. 9(d), at a certain Reynolds number, the maximum temperature, $T_{max,hs}$, of the H-MPF (single array) heat sink is lower than that of the NH-RM heat sink, and the difference is about 14 K, while the maximum temperature of the H-MPF (multiple array) heat sink is about 16 K lower than that of the NH-RM heat sink. It can be seen that the temperature uniformity of the H-MPF (multiple array) heat sink is greatly improved.

To achieve the same bottom temperature, the NH-RM heat sink needs a higher flow rate (or a bigger Reynolds number). For example, according to figs. 9(a) and 9(f), the NH-RM heat sink at Re = 600 has a similar maximum temperature of the bottom surface to the H-MPF (multiple array) heat sink at Re = 100. According to figs. 9(a) and 9(e), the maximum bottom temperature of the NH-RM heat sink with Re = 500 is similar to that of the H-MPF (single array) heat sink with Re = 100. In addition, it is worth mentioning that, as shown in figs. 9(g)-9(j), when Reynolds number is greater than 700, it can be found that the decrease rate of the maximum temperature of the bottom surface of the heat sink begins to slow down with the increase of Reynolds number.

Thermal performance analysis

Figure 10 illustrates the thermal performance parameters ($\Delta p_{max,ch}$, $\Delta p_{avg,ch}$, R_{tot}, P_{tot}, δT_{hs}, and δT_{bot}) of the NH-RM, H-MPF (single array), and H-MPF (multiple array) heat sinks as a function of Reynolds number (Re = 100-1000). In fig. 10(a), all three structures show an increase in $\Delta p_{max,ch}$ with increasing Reynolds number. Due to the presence of a pin fin array in the H-MPF heat sink, when the fluid-flows through this region, it significantly changes the flow regime of the fluid. When Re = 1000, compared with the NH-RM heat sink, the increase of the maximum pressure drop of the H-MPF (multiple array) heat sink is 17%, and the increase of the maximum pressure drop of the H-MPF (single array) heat sink is 15%.

Figure 10(b) presents the $\Delta p_{avg,ch}$ for the three types of heat sinks. While the NH-RM structure maintains a consistent pressure drop due to its uniform flow profile, both H-MPF (single array) and H-MPF (multiple array) exhibit similar pressure drop trends, with only a 1.2% difference between them for Re = 300.

In fig. 10(c), the R_{tot} decreases with increasing Reynolds number for all heat sink types. This is attributed to enhanced convective heat transfer at higher flow rates. The H-MPF structures outperform the NH-RM in reducing R_{tot} due to their superior hotspot cooling capability. Specifically, the H-MPF (multiple array) design achieves the lowest thermal resistance, with values 23% lower at Re = 100 and up to 39% lower at Re = 1000 compared to the NH-RM heat sink.

The total pumping power, P_{tot}, variation of the three heat sinks is shown in fig. 10(d). The total pumping power of the three heat sinks increases significantly with increasing Reynolds number. The pumping power of the H-MPF heat sink is higher than that of the NH-RM heat sink; this increase varies from 11% to 12.3% with increasing Reynolds number.

The variation of the three heat sinks including the MATD at the hotspot, δT_{hs}, and MATD at the bottom, δT_{bot}, is shown in figs. 10(e) and 10(f). The non-uniformity of temperature decreases as Reynolds number increases for both the hotspot and the bottom, because a larger Reynolds number reduces fluid hoarding and flow vortices in the channel. The MATD at the hotspot of the H-MPF (multiple array) heat sink is lower than that of the NH-RM heat sink, and this reduction varies from 25%-38% as Reynolds number increases from 100-1000. The MATD at the bottom of the H-MPF (multiple array) heat sink is lower than that of the NH-RM heat sink, and this reduction varies from 45%-53% as Reynolds number increases from

100-1000. The MATD of the H-MPF (multiple array) heat sink is lower than that of the H-MPF (single array) heat sink. Specifically, as Reynolds number increases from 100-1000, the MATD decreases from 8%-11.3% in the hotspots and from 9%-15% in the bottom areas.

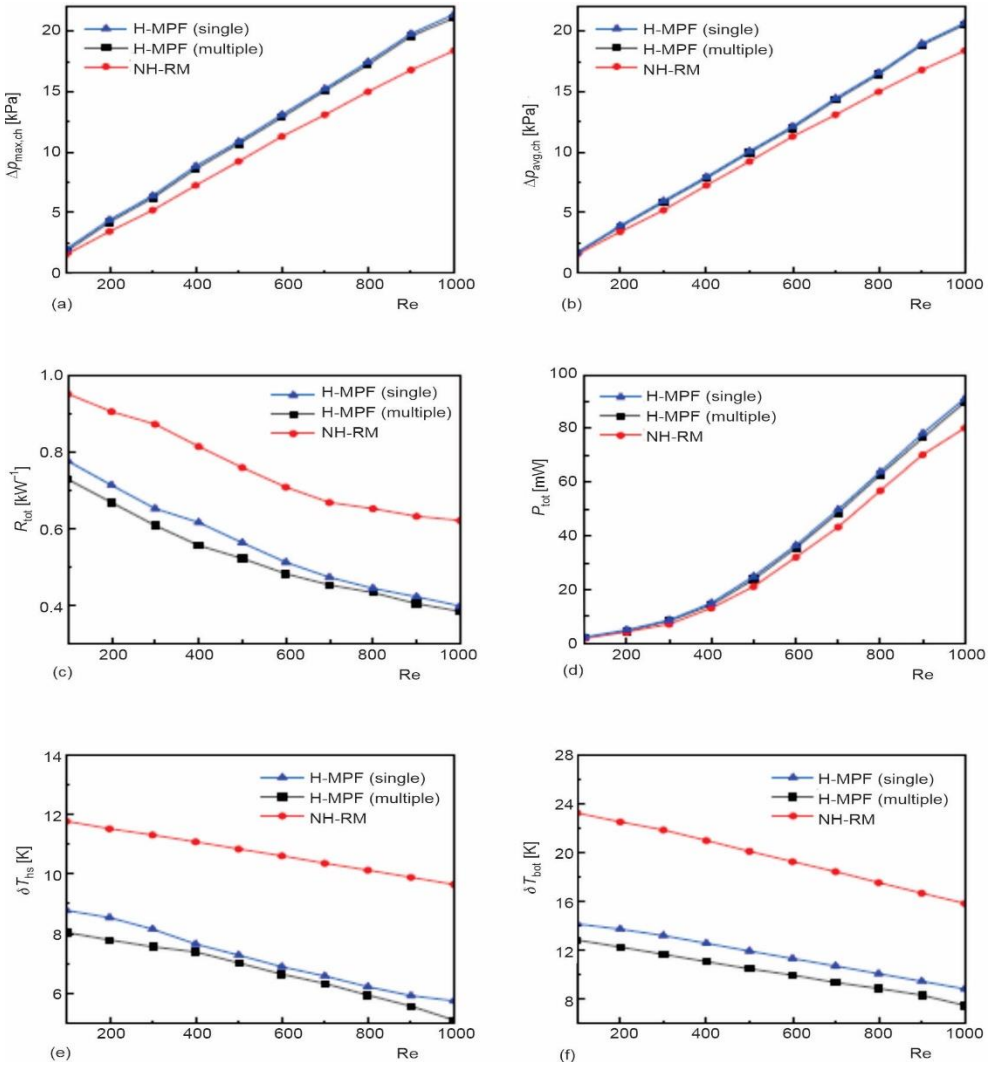

Figure 10. Variations of the performance parameters in the NH-RM, H-MPF (single array), and H-MPF (multiple array) heat sinks with Reynolds number; (a) the maximum pressure drop, (b) the average pressure drop, (c) total thermal resistance, (d) total pumping power, (e) MATD at the hotspot, and (f) MATD at the bottom

The variation trend of thermal performance

After analyzing the influence of Reynolds number on the performance of the heat sink, it is found that the variation trend of some performance parameters is different. Figure 11 illustrates the connection between these parameters. The variation of the total thermal resistance, R_{tot}, with the average pressure drop, $\Delta p_{avg,ch}$, is shown in fig. 11(a). It can be seen from fig. 11(a)

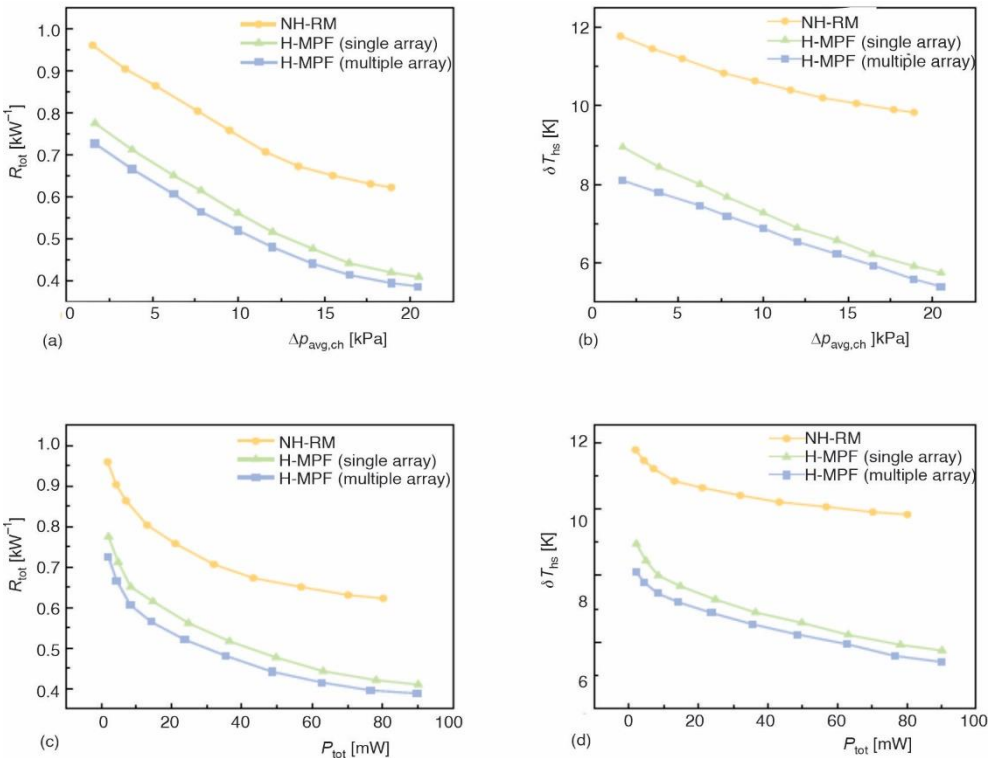

Figure 11. Variation link between heat sink performance parameters; (a) change of R_{tot} as $\Delta p_{avg,ch}$ increases, (b) change of δT_{hs} as $\Delta p_{avg,ch}$ increases, (c) change of R_{tot} as P_{tot} increases, and (d) change of δT_{hs} as P_{tot} increases

that the thermal resistance and the pressure drop of the heat sink show a negative correlation trend. As the pressure drop increases, the thermal resistance difference between the NH-RM heat sink and the H-MPF heat sink gradually becomes larger, while the pressure drop difference between the H-MPF (single array) heat sink and the H-MPF (multiple array) heat sink does not change basically.

The variation of the MATD at the hotspot, δT_{hs}, with the average pressure drop, $\Delta p_{avg,ch}$, is shown in fig. 11(b). The δT_{hs} of the three heat sinks decrease as the pressure drop increases. However, the difference of δT_{hs} between the H-MPF (single array) heat sink and the H-MPF (multiple array) heat sink decreases as the pressure drop increases.

The variation of the total thermal resistance, R_{tot}, and MATD at the hotspot, δT_{hs}, with the total pumping power, P_{tot}, is shown in figs. 11(c) and 11(d). Compared to the NH-RM heat sink, the H-MPF heat sink exhibits significantly lower R_{tot} and δT_{hs} at the same pumping power, and the reduction is gradually increased with the increase of pump power. The decrease of R_{tot} and δT_{hs} for the three heat sinks shows a nonlinear trend when P_{tot} increases. At low pumping power, the reduction rate of R_{tot} and δT_{hs} is higher as P_{tot} increases, but this rate gradually slows down as P_{tot} increases further.

Limiting power consumption test

Figure 12 illustrates the localized temperature profiles of the bottom surface of the NH-RM and H-MPF heat sinks at a specific Re = 1000 as the hotspot heat flux, q_{hs}, gradually increases

until it reaches the maximum temperature that the chip can withstand (95 °C), to explore the limit of processor power consumption that the heat sink can withstand (*z-x* plane, $y/L_y = 0$).

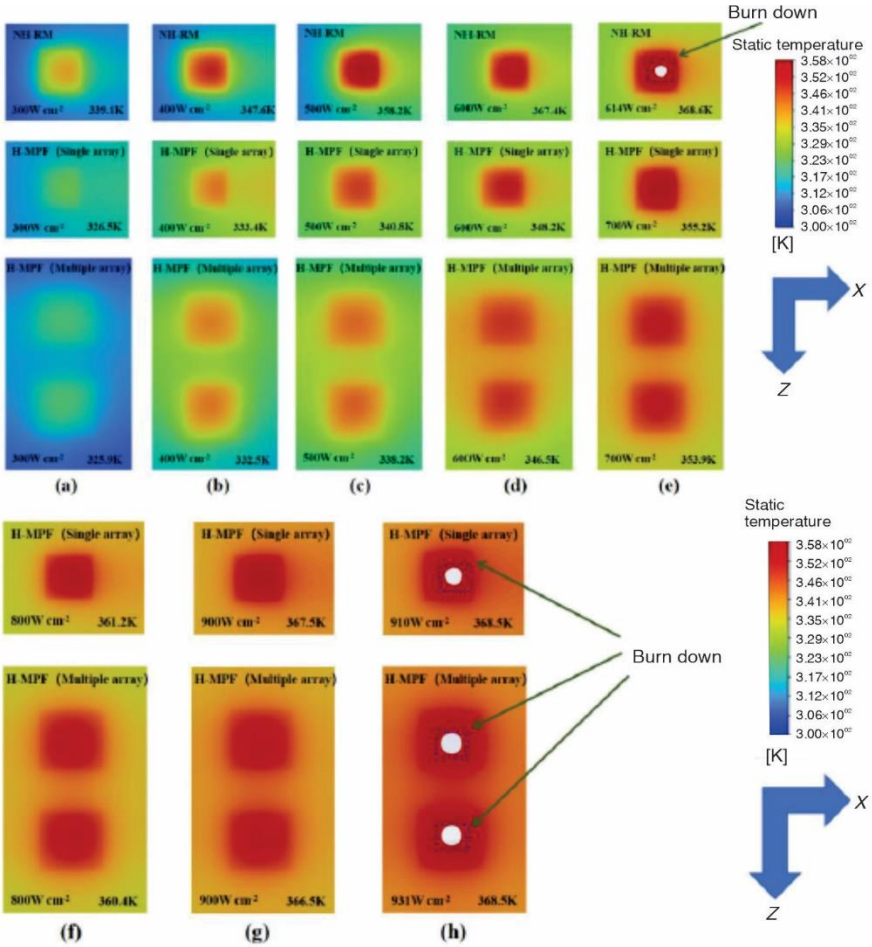

Figure 12. The bottom surface temperature distribution of the heat sink under different heat flux densities (*z-x* plane, $y/L_y = 0$), the maximum temperature of the hotspot, $T_{max,\,hs}$, is marked in the bottom right corner of each figure, the value of q_{hs} is marked in the lower left corner of each figure; (a) $q_{hs} = 300$ W/cm, (b) $q_{hs} = 400$ W/cm^2, (c) $q_{hs} = 500$ W/cm^2, (d) $q_{hs} = 600$ W/cm^2, (e) maximum heat flux of the NH-RM heat sink is 614 W/cm^2, and the heat flux of the H-MPF heat sink is set to 700 W/cm^2, (f) $q_{hs} = 800$ W/cm^2, (g) $q_{hs} = 900$ W/cm^2, (h) maximum heat flux of the H-MPF (multiple array) heat sink is 931 W/cm^2, and maximum heat flux of the H-MPF (single array) heat sink is set to 910 W/cm^2

Comparing the three heat sinks under the same heat flux density figs. 12(a)-12(e), it can be clearly seen that the isotherms of the H-MPF heat sink (especially the multiple array) are more dispersed, indicating that its heat diffusion ability is stronger and thus forms a more uniform temperature field at the bottom. As q_{hs} increases, $T_{max,\,hs}$ rise fastest for the NH-RM heat sink. For example, according to fig. 12(d), when q_{hs} is increased to 600 W/cm^2, $T_{max,hs}$ of NH-RM heat sink is already close to 95 °C, while $T_{max,\,hs}$ of both H-MPF heat sinks is still significantly below this limit at $q_{hs} = 700$ W/cm^2.

According to figs. 12(e) and 12(h), the maximum permissible heat flux of the NH-RM heat sink is 614 W/cm^2, the maximum permissible heat flux of the H-MPF (single array) heat sink is 910 W/cm^2, and the maximum permissible heat flux of the H-MPF (multiple array) heat sink is 931 W/cm^2. Compared to the NH-RM heat sink, the H-MPF (multiple array) increases the heat treatment capacity of the heat sink by more than 51% (from 614-932 W/cm^2). This is primarily attributed to the fact that the pin fin array significantly enhances the local convective heat transfer coefficient and the effective heat dissipation area in the hotspot region. The multiple array design further improves the limiting heat flux by about 3% (from 910-931 W/cm^2) compared to the single array design. This improvement mainly stems from the fact that the multiple array structure creates more and more evenly distributed fluid disturbances and secondary flows, optimizes the lateral heat diffusion below the cooling floor, and reduces the heat accumulation in the core area of the hotspot.

Entropy production analysis

The characteristic of energy loss is one of the important concerns in fluid-flow in a pipe. Compared with the traditional energy loss analysis method, entropy generation theory can better reflect the characteristics of energy loss and can reveal the relationship between energy dissipation and flow state in the flow field.

The entropy generation S consists of the heat transfer irreversible entropy production S_t and the fluid friction irreversible entropy production S_f. The expression for S is as [32, 33]:

$$S = \frac{q^2 \pi D_{\mathrm{h}}^2}{k T_{\mathrm{f,ave}}^2 \mathrm{Nu}} + \frac{32 m^3 f}{\pi^2 \rho^2 T_{\mathrm{f,ave}} D_{\mathrm{h}}^5} = S_t + S_f \tag{11}$$

where $T_{\mathrm{f,ave}}$ is the average temperature of the fluid and f – the coefficient of friction, which is expressed as:

$$f = \frac{\left(\frac{\Delta P}{L}\right) D_{\mathrm{h}}}{2\rho v^2} \tag{12}$$

where q‘ and r can be given as:

$$q' = 2\pi r q, \quad r = \frac{D_{\mathrm{h}}}{2} \tag{13}$$

For pure rectangular micro-channels, such as the NH-RM heat sink, f_0 and Nu_0 are benchmarks in this paper to normalize the friction coefficient and Nusselt number. The baseline entropy generation, S_0, can be given as:

$$S_0 = S_{t,0} + S_{f,0} = \frac{q^2 \pi D_{\mathrm{h}}^2}{k T_{\mathrm{f,in}}^2 \mathrm{Nu}_0} + \frac{32 m^3 f_0}{\pi^2 \rho^2 T_{\mathrm{f,in}} D_{\mathrm{h}}^5} \tag{14}$$

Figure 13 illustrates the variation of the heat transfer performance $\mathrm{Nu}/\mathrm{Nu}_0$. It can be seen that the $\mathrm{Nu}/\mathrm{Nu}_0$ ranges from 1.35-4.15 for all cases, and increases with the increase of Reynolds number. When Re = 100, $\mathrm{Nu}/\mathrm{Nu}_0$ is minimized for both heat sinks, but the difference in $\mathrm{Nu}/\mathrm{Nu}_0$ between the two heat sinks gradually decreases with further increase in Reynolds number. The above phenomenon is that the increase in $\mathrm{Nu}/\mathrm{Nu}_0$ by different heat sinks is less affected by high Reynolds number values. The $\mathrm{Nu}/\mathrm{Nu}_0$ is larger for the H-MPF (multiple array) than the H-MPF (single array) heat sink, and the $\mathrm{Nu}/\mathrm{Nu}_0$ gradually becomes similar for both as Reynolds number increases from 600-1000.

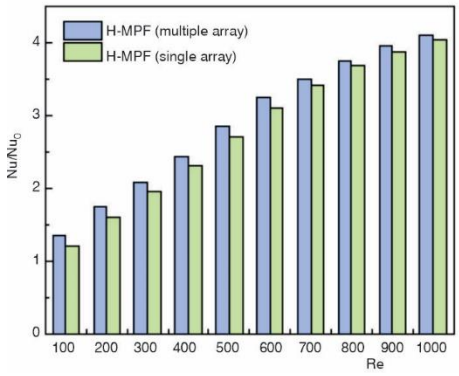

Figure 13. Variation of Nu/Nu$_0$ in different heat sinks with Reynolds number

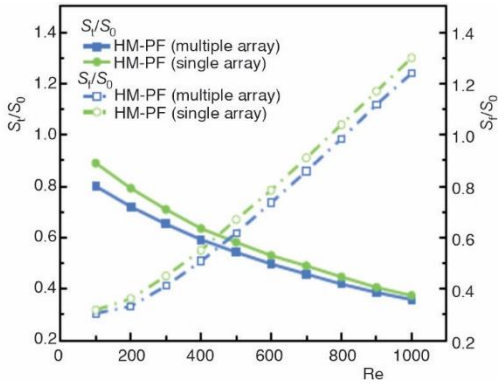

Figure 14. Variation of S_t/S_0 and S_f/S_0 in different heat sinks with Reynolds number

To further study the comprehensive cooling performance of the new heat sink, the S/S_0 is analyzed, which consists of two parts, S_t/S_0 and S_f/S_0, where a larger S/S_0 indicates a larger useful power loss of the new heat sink. According to eqs. (11) and (14), the trend of S_t/S_0 is opposite to Nu/Nu$_0$, which decreases with the increase of Reynolds number. The trend of S_f/S_0 is consistent with f/f_0, which increases with the growth of Reynolds number, as shown in fig. 14. At Re = 100, the value of S_f/S_0 is very small (close to 0), while the value of S_t/S_0 is significantly larger than 1, and S_t/S_0 accounts for more than 95% of the total S/S_0. This means that at low flow rates, the irreversibility of the system is almost entirely driven by the heat transfer temperature difference. At Re = 1000, the value of S_t/S_0 has dropped to close to 1, while S_f/S_0 has risen to a value much larger than 1, S_f/S_0 becomes the dominant term, accounting for more than 85% of the total S/S_0, which indicates that at high flow rates, the irreversibility of the system mainly comes from the pump work consumed to overcome the flow resistance. As shown in fig. 14, S_f/S_0 and S_t/S_0 are basically the same in the interval Re = 400-500, S reaches its relative minimum around this interval, and operating under this Reynolds number minimizes the total entropy generation while achieving the optimal efficiency of the operation.

Comparison of the heat dissipation effects of refrigerants

Phase transition simulation method and setting

In the multiphase flow model, the VoF model is selected. This model is well-suited for tracking the clear liquid-vapor interface and simulates the phase transition process effectively. The main phase (Phase 1) is liquid refrigerant, and the second phase (Phase 2) is refrigerant vapor. We choose the Lee model as the phase transition model, and the phase transition rate is driven by the difference between the unit temperature and the saturation temperature. The Lee model calculates the mass transfer rate using:

Mass transfer equation

$$\frac{\partial}{\partial t}\left(\alpha_{\mathrm{v}}\rho_{\mathrm{v}}\right)+\nabla\left(\alpha_{\mathrm{v}}\rho_{\mathrm{v}}\vec{V}_{\mathrm{v}}\right)=m_{\mathrm{lv}}-m_{\mathrm{vl}} \tag{15}$$

where α_{v} is the vapor phase volume fraction, ρ_{v} – the vapor phase density, V_{v} – the vapor phase velocity, and m_{lv}, m_{vl} – the mass transfer rates during the evaporation and condensation processes. Evaporation process (when the temperature of the liquid phase T_{l} is higher than the saturation temperature T_{sat}):

$$m_{lv} = coeff \ \alpha_l \rho_l \frac{(T_l - T_{sat})}{T_{sat}} \tag{16}$$

Condensation process (when the temperature of the vapor phase T_v is lower than the saturation temperature T_{sat}):

$$m_{vl} = coeff \ \alpha_v \rho_v \frac{(T_{sat} - T_v)}{T_{sat}} \tag{17}$$

where *coeff* is the phase transition relaxation coefficient, T_l – the liquid phase temperature, T_v – the vapor phase temperature, and T_{sat} – the saturation temperature (300 K)

After conducting a sensitivity test, the *coeff* was set to 0.1 s^{-1}. This value ensures the stable progress of the phase transformation process and avoids excessive numerical instability. The physical properties of each refrigerant at a saturation temperature of 300 K are listed in tab. 3 and are set as constants. The inlet is a saturated liquid at 300 K ($\alpha_l = 1$). The bottom heat flux density is consistent with the single-phase simulation; the entire computational domain is initialized as a saturated liquid at 300 K.

Table 3 The physical property parameters of refrigerants

	T_s [K]	ρ_l [kgm^{-3}]	ρ_v	C_{pl} [kJkg^{-1}K^{-1}]	C_{pv}	H_{lv} [kJkg^{-1}]	k_l [Wm^{-1}K^{-1}]	k_v
R1234yf	300	1085.1	39.98	1.40	1.06	143.86	62.97	14.05
R1234ze(E)	300	1157.0	27.82	1.39	0.98	165.51	73.59	13.75
R600a	300	548.3	9.61	2.44	1.81	326.87	88.60	17.02

Phase transition simulation results and discussion

Considering the current practical refrigerant applications, this study additionally selected two common green refrigerants, R1234yf and R1234ze(E), as well as a hydrocarbon refrigerant, R600a, to conduct a heat dissipation comparison. To ensure the boiling phase change, both the inlet temperature and the saturation temperature of the refrigerants are set at 300 K. At a saturation temperature of 300 K, the physical property parameters of these refrigerants are shown in tab. 3.

Figure 15 illustrates the temperature distribution of the refrigerant at the bottom of the heat sink (*z-x* plane, $L_y/y = 0$) in the range of Reynolds number from 200-1000. For organic refrigerants under the same flow rate conditions, R1234ze(E) demonstrates superior heat dissipation performance. The average maximum temperature on the bottom surface of the heat exchanger is approximately 3 K lower than that of R1234yf, which is similar to the previous experimental results of Xu *et al*. [13]. However, due to the lower vapor density and higher latent heat of vaporization, under the same flow rate conditions, the average maximum temperature at the bottom surface of the heat sink was reduced by 8 K when using R600a compared to R1234yf, and by 5 K compared to R1234ze(E).

Figure 16 illustrates the changes in the liquid phase at the cross-section of the flow channel when using R600a, and the Reynolds number increases from 800-1000. It can be seen that at this point, the phase change within the flow channel remains almost unchanged as Reynolds number increases, and the phase change has almost reached saturation. As shown in figs. 16(d) and 16(e), when Reynolds number increases from 800-1000, the maximum bottom temperature of the heat sink only decreases by 1 K. At this point, further increasing the flow rate will reduce the efficiency.

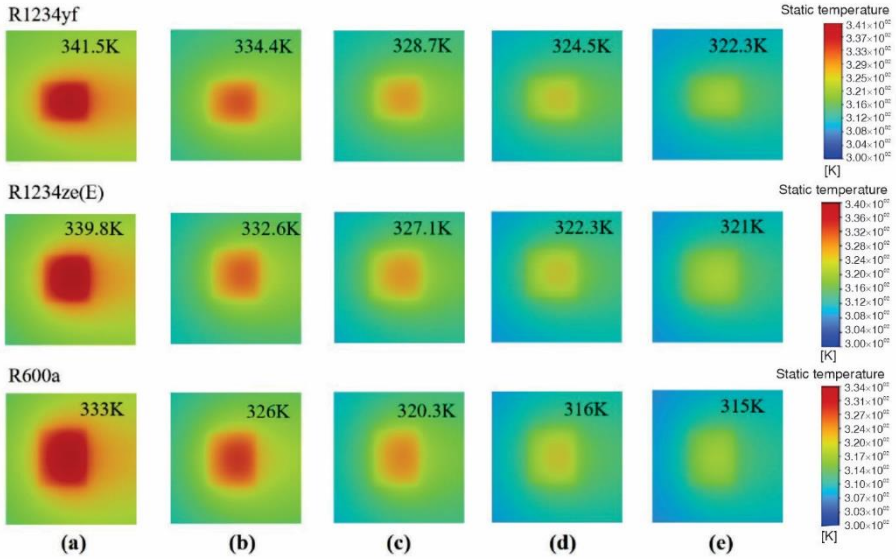

Figure 15. The temperature distribution at the bottom of the heat sink (*z-x* plane, $L_y/y = 0$) of the refrigerants at different Reynolds number; (a) Re = 200, (b) Re = 400, (c) Re = 600, (d) Re = 800, and (e) Re = 1000

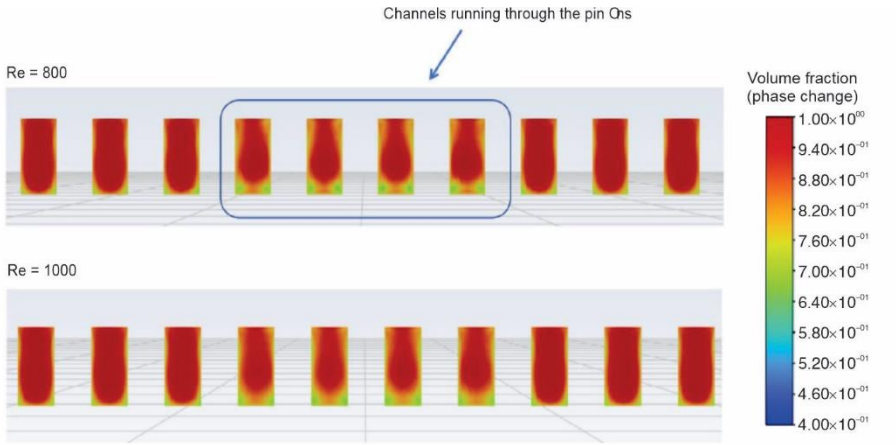

Figure 16. The changes in the flow channel cross-sectional liquid phase when the Reynolds number increases from 800-1000 while using R600a

This study compared the phase change cooling performance of different refrigerants under a fixed saturation temperature (300 K). However, during actual system operation, the saturation pressure and the subcooling degree may change. Therefore, the phase change results obtained in this study were under specific operating conditions, and relevant experimental verification is required before the deployment of the actual processor cooling system. Within the conventional pressure range (corresponding to saturation temperatures of 280-320 K), the heat dissipation performance ranking of the refrigerants remains stable. However, a significant increase in pressure may reduce the density ratio advantage of R600a; while an increase in supercooling degree will enhance the advantage of R600a due to its high liquid phase heat capacity

and thermal conductivity. In practical design, it is recommended to verify based on the specific physical properties of the target operating range.

Discussion on refrigerants

The performance advantage of R600a in phase change cooling (5-8 K lower than HFO) can be attributed to its unique physical properties combination, especially its high latent heat of vaporization, superior density ratio, and low surface tension. The latent heat of vaporization of R600a (326.87 kJ/kg) is about 2.3 times that of R1234yf (143.86 kJ/kg). Under the same mass flow rate and saturation condition, R600a per unit mass can absorb and transfer more heat.

The density ratio of R600a ($\rho_l/\rho_v \approx 57$) is much higher than that of R1234yf ($\rho_l/\rho_v \approx 27$) and R1234ze(E) ($\rho_l/\rho_v \approx 42$). When changing from liquid to vapor phase, the volume expansion of R600a is more dramatic, which can more effectively separate the heated liquid and the forming bubbles, thus enhancing the flow disturbance. A higher density ratio means that the bubble is subjected to more significant buoyancy during growth, which is beneficial for the bubble to escape from the wall faster.

The surface tension of R600a is lower than that of the two HFO, which facilitates the generation of a smaller size and a larger number of bubbles, thus significantly increasing the effective vapor-liquid interface heat transfer area.

According to ASHRAE Standard 34-2024, R600a is classified as A3 (highly combustible) refrigerant. In contrast, R1234yf and R1234ze(E) are in class A2L (slightly combustible), and direct use of R600a in data centers or any enclosed or semi-enclosed electronic equipment in the presence of high thermal surfaces typically requires safety systems. All three are environmentally friendly refrigerants (low GWP, zero ODP). However, HFO currently face patent and cost challenges, while R600a, as a mature hydrocarbon working fluid, usually has lower costs.

In practice, it is necessary to consider the environment, safety, performance, cost, and other factors to select refrigerants. For example, on specific occasions with high heat dissipation performance requirements and safety conditions, R600a is still an important option.

Conclusions

In this study, the numerical simulation method was adopted to conduct a detailed comparative study on the thermal performance of a H-MPF (single array) heat sink, a H-MPF (multiple array) heat sink, and a micro-channel heat sink. Additionally, the cooling performance of several commonly used refrigerants was assessed, leading to the following conclusions.

- Numerical simulations show that the H-MPF (multiple array) heat sink demonstrates significant thermal performance enhancements compared to the NH-RM heat sink. At Re = 100, the H-MPF (multiple array) heat sink reduces the hotspot temperature rise by 25%, non-uniformity of temperature by 32% (hotspot) and 45% (common), and overall thermal resistance by 23%. As Reynolds number increases to 1000, these improvements become more pronounced. Compared to the H-MPF (single array) heat sink, the H-MPF (multiple array) maintains nearly identical pressure drop and pumping power, while reducing R_{tot} and S by a maximum of 4% and 7% at Re = 400, respectively. Furthermore, H-MPF (multiple array) heat sink offers significantly improved non-uniformity of temperature, with a maximum reduction of 12% in the hotspot area at Re = 200 and 16% in the common area at Re = 300.
- Based on the heat flux analysis, the H-MPF (multiple array) heat sink can improve the limiting heat flux at the hotspot by 51% compared with the NH-RM heat sink and 3% compared with the H-MPF (single array) heat sink at Re = 1000, while keeping the maximum temperature below the limit.

- The core advantage of the H-MPF (multiple array) heat sink is the significant reduction of the irreversible heat transfer loss S_t. At low Reynolds number (Re = 100), S_t contributes more than 95% of the total entropy generation. As Reynolds number increases, S_f becomes dominant, accounting for more than 85% at Re = 1000. The H-MPF (multiple array) heat sink further reduces the total entropy generation S by 4% to 7% in the range of Reynolds number from 100-1000. The total entropy generation S reaches a relative minimum in the interval of Reynolds number from 400-500.
- The simulation results show that the refrigerant with low vapor density and high latent heat of vaporization has superior cooling performance. This is attributed to the fact that the high latent heat of vaporization improves the heat-carrying capacity of the fluid per unit mass, while the low vapor density promotes the bubble detachment and flow mixing. Therefore, in this study, a reference criterion for the selection of refrigerants for the phase change cooling system with high heat flux is put forward: The refrigerant with high latent heat of vaporization and low vapor density is preferred.

Declaration of interest statement

Authors declare no conflicts of interests in this paper.

Acknowledgment

This work was supported by Natural Science Foundation of Shandong Province, China (Grant No. ZR2024QE263), College Youth Innovation Team of Shandong Province, China (Grant No. 2024KJH151), Young Talent of Lifting Engineering for Science and Technology in Shandong, China (Grant No. SDAST2024QTA048, SDAST2025QTA047) and Key R & D Program of Shandong Province, China (2022CXGC020901).

Nomenclature

A_c – cross-sectional area of a channel [m^2]
A_{hs} – cross-sectional area of a hotspot [m^2]
C_p – specific heat capacity [$Jkg^{-1}K^{-1}$]
D_h – hydraulic diameter [m]
g – gravitational acceleration [ms^{-2}]
H_b – height of bottom [m]
H_c – height of micro-channel [m]
k – thermal conductivity [$Wm^{-1}K^{-1}$]
L_x,L_y,L_z – overall length, width, and height of the heat sink, respectively [m]
L_p – length of processor [m]
m – molar mass (physics) [$kgmol^{-1}$]
MATD – mean absolute temperature deviation [K]
Nu – Nusselt number
n_{ch} – total number of channels
P_{tot} – total pumping power required for the heat sink [W]
$\Delta p_{max,ch}$ – maximum pressure drop of the channels [Pa]
$\Delta p_{avg,ch}$ – average pressure drop of the channels [Pa]
Q_{tot} – total heat applied to heat sinks [W]
q_c – heat flux applied to the common area [Wcm^{-2}]
q_{hs} – heat flux applied to the hotspot area [Wcm^{-2}]
Re – Reynolds number
R_{tot} – total thermal resistance [KW^{-1}]
S – entropy production [WK^{-1}]
S_t – heat transfer irreversible entropy generation [WK^{-1}]
S_f – friction irreversible entropy generation [WK^{-1}]
S_c – spacing of channel [m]
T – temperature [K]
$T_{f,in}$ – fluid inlet temperature [K]
$T_{max,s}$ – maximum temperature at the base of the heat sink [K]
$T_{max,hs}$ – maximum temperature at the hotspot [K]
$T_{min,hs}$ – minimum temperature at the hotspot [K]
$T_{avg,hs}$ – average temperature at the hotspot [K]
$\Delta T_{max,hs}$ – maximum temperature rise at the hotspot [K]
δT_{hs} – MATD at the hotspot [K]
δT_{bot} – MATD at the bottom (hotspot + common) [K]
u_{avg} – average inlet velocity of fluid [ms^{-1}]
W_c – width of channel [m]
W_p – width of processor [m]

Greek symbols

μ – viscosity [Pa s]
ρ – density [kgm^{-3}]

Acronym

H-MPF – hybrid micro-channel-pin fin heat sink
NH-RM – non-hybrid rectangular micro-channel heat sink

References

[1] Kwon, H., *et al*., Capillary-Enhanced Two-Phase Micro-Cooler Using Copper-Inverse-Opal Wick with Silicon Micro-channel Manifold for High-Heat-Flux Cooling Application, *International Communications in Heat and Mass Transfer, 156* (2024), 107592
[2] Fazeli, K., Vafai, K., Analysis of Optimized Combined Micro-channel and Heat Pipes for Electronics Cooling, *International Journal of Heat and Mass Transfer, 219* (2024), 124842
[3] Hu, C., *et al*., Research on Heat Transfer and Flow Distribution of Parallel-Configured Micro-channel Heat Sinks for Arrayed Chip Heat Dissipation, *Applied Thermal Engineering, 255* (2024), 124003
[4] Zhou, L., *et al*., Numerical Study on Infrared Detectors Cooling by Multi-Stage Thermoelectric Cooler Combined with Micro-channel Heat Sink, *Applied Thermal Engineering, 236* (2024), 121788
[5] Cao, B., Wu, Z., Micro-channel Heat Sinks for Hotspot Thermal Management: Achieving Minimal Pressure Drop and maximal thermal performance, *International Journal of Heat and Mass Transfer, 236* (2025), 126411
[6] Dong, W., *et al*., Research Progress on Passive Enhanced Heat Transfer Technology in Micro-channel Heat Sink, *International Journal of Heat and Mass Transfer, 220* (2024), 125001
[7] Shang, H., *et al*., Comprehensive Review of Enhancement Techniques and Mechanisms for Flow Boiling in Micro/Mini-Channels, *Applied Thermal Engineering, 258* (2025), 124783
[8] Zhao, C., *et al*., A Critical Review of the Preparation Strategies of Thermally Conductive and Electrically Insulating Polymeric Materials and their Applications in Heat Dissipation of Electronic Devices, *Advanced Composites and Hybrid Materials, 6* (2022), 27
[9] Yang, M, *et al*., Experimental Study on Single-Phase Hybrid Micro-channel Cooling Using HFE-7100 for Liquid-Cooled Chips, *International Journal of Heat and Mass Transfer, 160* (2020), 120230
[10] Kim, J., *et al*., Computational Study of Single-Phase Immersion Cooling for High-Energydensity Server Rack for Data Centers, *Applied Thermal Engineering, 264* (2025), 125476
[11] Su, Z., Mesoscale Multi-Component Energy Density Transport for Natural Convective Microchip Cooling with Solid-Liquid-Gas Phase Changes, *Applied Thermal Engineering, 236* (2024), 121808
[12] Moradikazerouni, A., Heat Transfer Characteristics of Thermal Energy Storage System Using Single and Multi-Phase Cooled Heat Sinks: A Review, *Journal of Energy Storage, 49* (2022), 104097
[13] Xu, Z., *et al*., Experimental Investigations of the Flow Boiling Characteristics of Green Refrigerants in a Novel Petaloid Micropin-Fin Heat Sink, *Int. Journal of Heat and Mass Transfer, 212* (2023), 124243
[14] Rostami, S., *et al*., Numerical Assessment of the Multi-Phase Nanofluid-flow Inside a Micro-channel During the Melting and Solidification of PCM in the Thermal Management of a Heatsink, *Engineering Analysis with Boundary Elements, 148* (2023), Mar., pp. 267-278
[15] Deng, M., *et al*., A Graphene Nanoflake-Based Flexible Composite Phase Change Material for Enhanced Heat Dissipation in Chip Cooling, *Applied Thermal Engineering, 245* (2024), 122908
[16] Patel, A., *et al*., Multi-Chip Jet Impingement Cooling for Heat Dissipation in 2.5D Integrated System with 1 kW+ Thermal Design Power, *International Journal of Heat and Mass Transfer, 244* (2025), 126978
[17] Deng, Z., *et al*., Thermal Analysis and Optimization of High-Power GPUs from Heat Sinks to Package Interfaces, *Applied Thermal Engineering, 280* (2025), 128008
[18] Zhao, J., *et al*., Numerical Study and Optimizing on Micro Square Pin-Fin Heat Sink for Electronic Cooling, *Applied Thermal Engineering, 93* (2016), Jan., pp. 1347-1359
[19] Li, P., *et al*., Flow and Heat Transfer Characteristics and Optimization Study on the Water-Cooled Micro-channel Heat Sinks with Dimple and Pin-Fin, *International Journal of Heat and Mass Transfer, 119* (2018), Apr., pp. 152-162
[20] Ansari, D., Kim, K.-Y., Hotspot Thermal Management Using a Micro-channel-Pinfin Hybrid Heat Sink, *International Journal of Thermal Sciences, 134* (2018), Dec., pp. 27-39
[21] Vilarrubí, M., *et al*., Experimental and Numerical Study of Micro-Pin-Fin Heat Sinks with Variable Density for Increased Temperature Uniformity, *International Journal of Thermal Sciences, 132* (2018), Oct., pp. 424-434

[22] Feng, S., *et al*., Thermal Management of 3D Chip with Non-Uniform Hotspots by Integrated Gradient Distribution Annular-Cavity Micro-Pin Fins, *Applied Thermal Engineering, 182* (2021), 116132
[23] Wang, G., *et al*., Thermal Hydraulic Performance of Tree-Like Micro-channel Heat Sink with High Branching Level Based on the Improved Murray's Law, *International Journal of Heat and Mass Transfer, 231* (2024), 125875
[24] Danismaz, M.,Geometric Analysis of Pin Fin Heat Sinks: Effects of Ellipticity and Perforation for Fin on Heat Transfer, *Case Studies in Thermal Engineering, 74* (2025), 106918
[25] Shafeie, H., *et al*., Numerical Study of Heat Transfer Performance of Single-Phase Heat Sinks with Micro Pin-Fin Structures, *Applied Thermal Engineering, 58* (2013), 1-2, pp. 68-76
[26] Yeom, T., *et al*., Enhanced Heat Transfer of Heat Sink Channels with Micro Pin Fin Roughened Walls, *International Journal of Heat and Mass Transfer, 92* (2016), Jan., pp. 617-627
[27] Wiriyasart, S., Naphon, P., Liquid Impingement Cooling of Cold Plate Heat Sink with Different Fin Configurations: High Heat Flux Applications, *International Journal of Heat and Mass Transfer, 140* (2019), Sept., pp. 281-292
[28] Fu, L., *et al*., Geometric Multi-Objective Optimization of a Micro-channel-Pinfin Hybrid Heat Sink, *International Journal of Thermal Sciences, 211* (2025), 109711
[29] Qu, W., Experimental and Numerical Study of Pressure Drop and Heat Transfer in a Single-Phase Micro-Channel Heat Sink, *International Journal of Heat and Mass Transfer, 45* (2002), 12, pp. 2349-2465
[30] Harris, M., *et al*., Assessing Thermohydraulic Performance in Novel Micro Pin-Fin Heat Sinks: A Synergistic Experimental, Agile Manufacturing, and Machine Learning Approach, *International Journal of Heat and Mass Transfer, 239* (2025), 126581
[31] Reddy, S. R., Dulikravich, G. S., Inverse Design of Cooling of Electronic Chips Subject to Specified Hot Spot Temperature and Coolant Inlet Temperature, *Proceedings*, 12th International Conference on Nanochannels, Micro-channels, and Minichannels, San Francisco, Cal., USA, 2015
[32] Li, P., *et al*., Heat Transfer Enhancement, Entropy Generation and Temperature Uniformity Analyses of Shark-Skin Bionic Modified Micro-channel Heat Sink, *International Journal of Heat and Mass Transfer, 146* (2020), 118846
[33] Bejan, A., A Study of Entropy Generation in Fundamental Convective Heat Transfer, *Journal of Heat Transfer, 101* (1979), 4, pp. 718-725

Paper submitted: November 28, 2025
Paper revised: January 10, 2026
Paper accepted: January 16, 2026
2026 Published by the Vinča Institute of Nuclear Sciences, Belgrade, Serbia.
This is an open access article distributed under the CC BY 4.0 terms and conditions.